

# Land-Locked Convection as a Barrier to MJO Propagation across the Maritime Continent

A. Savarin<sup>1</sup> and S. S. Chen<sup>1</sup>

<sup>1</sup>University of Washington

## Key Points:

- Land and land-sea contrast weaken the MJO and disrupt its propagation over the Maritime Continent.
- Land-sea contrast of MC islands induces a strong diurnal cycle with strong land-locked convection in the afternoon.
- Mountains are less disruptive to MJO propagation than larger and stronger land-locked convective systems that form over land without them.

## Abstract

Large-scale convection associated with the Madden-Julian Oscillation (MJO) initiates over the Indian Ocean and propagates eastward across the Maritime Continent (MC). Over the MC, MJO events are generally weakened due to complex interactions between the large-scale MJO and the MC landmass. The MC barrier effect is responsible for the dissipation of 40-50% of observed MJO events and is often exaggerated in weather and climate models. We examine how MJO propagation over the MC is affected by two aspects of the MC - its land-sea contrast and its terrain.

To isolate the effects of mountains and land-sea contrast on MJO propagation, we conduct three high-resolution coupled atmosphere-ocean model experiments: 1) control simulation (CTRL) of the 2011 November-December MJO event, 2) flattened terrain without MC mountains (FLAT), and 3) no-land simulation (WATER) in which the MC islands are replaced with 50 m deep ocean. CTRL captures the general properties of the diurnal cycle of precipitation and MJO propagation across the MC. The WATER simulation produces a more intense and smoother-propagating MJO compared with that of CTRL. In contrast, the FLAT simulation produces much more convection and precipitation over land (without mountains) than CTRL, which results in a stronger barrier effect on MJO propagation. The land-sea contrast induced land-locked convection weakens the MJO's convective organization. The land-locked convective systems over land in FLAT are more intense, grow larger, and last longer, which is more detrimental to MJO propagation over the MC, than the mountains that are present in CTRL.

## Plain Language Summary

An MJO event, which consists of an eastward propagating coupling between large-scale convection and precipitation, does not meet much resistance before reaching the islands of the Indonesian Maritime Continent. Once it does, its propagation gets disrupted, and many MJOs weaken or even completely dissipate over the region. The definitive reasons behind this behavior have not been established, though many studies point to the importance of the land-sea contrast and highly variable terrain within the region. Our study investigates the relative effects that terrain and land-sea contrast have on MJO propagation with the use of a high-resolution atmosphere-ocean coupled model where we first simulate an MJO event with real topography. Then we first flatten the topography and then remove land altogether to see the individual effects of topography and air-sea interaction, respectively. Without land, the MJO propagates through the region without disruption, so presence of land is detrimental to MJO propagation, and in the simulation with real topography, the disruption is smaller with realistic topography. In the simulation without mountains, diurnal systems that form over land can grow into large-scale systems with their own circulations and compete with the MJO.

## 1 Introduction

The Maritime Continent (MC) is a unique region of thousands of islands in the tropical Pacific warm pool with a very dynamic distribution of topography and terrain, and one of the main drivers of the global general circulation (Ramage, 1968). It lies at the intersection of many scales of atmospheric and oceanic variability, from decadal (El Niño - Southern Oscillation), to seasonal (monsoons), intraseasonal (the Madden-Julian Oscillation (MJO), Madden & Julian, 1971, 1972), and some of the strongest diurnal cycles in the world (Moron et al., 2015). Kikuchi and Wang (2008) classify the DC over the MC into the coastal regime under which systems of land- and sea-breezes drive precipitation location and intensity, modified by the background circulation, orography, and coastline orientation (Abbs & Physick, 1992). Differential solar heating during the day induces a sea breeze circulation around islands and precipitation begins to form on the coast, then propagate inland from noon to evening; precipitation over the neighboring oceans is suppressed (Miller et al., 2003). At night and in the early morning, the land breeze, which is associated with weaker precipitation, propagates offshore and suppresses precipitation on the coast (Chen & Houze Jr, 1997).

Numerical models often underestimate the precipitation in this region, in part due to a poor representation of the DC of precipitation around the islands (Neale & Slingo, 2003). Increasing the model resolution reduces the dry bias over the MC and has been linked to better-resolved surface conditions and land-sea contrast (Schiemann et al., 2014), but models are still too quick to trigger precipitation over land and exaggerate the amplitude of the DC over land compared to what is simulated over water (Lee & Wang, 2021; Li et al., 2017; Love et al., 2011).

The MC acts as an obstacle to the eastward propagation of the MJO from the Indian Ocean toward the western Pacific - its barrier effect is responsible for weakening most MJO events that cross the region, and completely dissipating 45-50% of them (Kerns & Chen, 2020; C. Zhang & Ling, 2017). Some studies focus on the physical effect related to the blocking of flow by topography (e.g., Wu & Hsu, 2009), and its direct consequences such as reduced air-sea fluxes over islands compared to the surrounding ocean (Sobel et al., 2010; Birch et al., 2016). More studies focus on dynamical barriers to MJO propagation, such as the westward propagation of dry air that meets the MJO over the MC (DeMott et al., 2018; Feng et al., 2015), the Warm Pool Dipole (L. Zhang & Han, 2020), and recently, the DC has been identified as an important contributor (e.g., Hagos et al., 2016; Ling, Zhang, et al., 2019). The MC barrier effect is exaggerated in most general circulation models (Ling, Zhao, & Chen, 2019), leading to a prediction barrier to the MJO. As one of the largest sources of tropical intraseasonal predictability, the MJO's downstream influences cannot be accurately resolved without capturing its propagation (or dissipation) over the MC.

The influence of the MJO on the DC over the MC is clear and can be explained by an influx of surface westerly winds which increase convergence, and a large supply of moisture that both accompany the active MJO (Lu et al., 2019). Rauniyar and Walsh (2011) and Oh et al. (2012) found that during the active phase of the MJO precipitation over water is increased, but precipitation over land is reduced, and the timing of peak precipitation is delayed. The DC of deep convective clouds was found to be amplified during active MJO over both land and water (B. Tian et al., 2006), but Peatman et al. (2014) show that over the islands of the MC, outgoing longwave radiation is no longer a good proxy for precipitation. Peatman et al. (2014) and Sakaeda et al. (2017) also note that the strongest DC is seen in the convectively suppressed conditions before the arrival of active precipitation, when the skies are most cloud-free. All these results show that the MJO is carried through the MC over water (C. Zhang & Ling, 2017).

The influence of the DC on MJO propagation is more difficult to infer, but land convection is frequently identified as the main culprit for the MC barrier effect related

to the DC. Ling, Zhang, et al. (2019) find that one factor that separates crossing MJOs from those that dissipate is a strong increase in the DC ahead of precipitation (as described by Peatman et al., 2014). This increases soil moisture ahead of the MJO and dampens the land DC during active MJO - more so for crossing MJO events than the ones that dissipate. C. Zhang and Ling (2017) come to a similar conclusion in a different manner - they suggest that the inhibition of convective development over water could be the reason behind the barrier effect. The MC barrier effect seems to be strengthened either when precipitation over land is strong, or when precipitation over water is weak - or both.

Most other studies focusing on the MC barrier effect rely on modeling, where parameters are changed, and their effects examined. The observations of an enhanced DC of precipitation ahead of the active MJO are reproduced in cloud-resolving simulations, while topography plays a role in where precipitation develops and varies among islands (Wei et al., 2020). Inness and Slingo (2006) find that at low resolution, topography as a physical barrier is more important than the presence of islands themselves. But at higher resolution, many studies that modify the DC in one way or another find that weakening the diurnal cycle over land leads to a weaker barrier to MJO propagation (e.g., Hagos et al., 2016; Oh et al., 2013; H. Tan et al., 2022; Zhou et al., 2021).

Though some studies have already performed similar terrain modifications as what we show here (H. Tan et al., 2022; Zhou et al., 2021), we go a step further and separate the effects of MC topography from the effects of its DC and land-sea contrast and identify physical processes through which those impact MJO propagation. The modeling configuration, MJO tracking, and our unique way of analyzing the DC of precipitation are described in Section 2. Section 3 focuses on applying the methods to 20 years of precipitation data to establish baseline differences in the DC of precipitation between MJO and non-MJO environments. Section 4 addresses the MJO characteristics, while Section 5 describes the DC differences between the model simulations and observations. In Section 6, we establish enhanced land-locked convection as a physical mechanism that strongly contributes to the weakening of the MJO over the MC. The results are summarized in Section 7.

## 2 Methods and Data

### 2.1 Model Configuration and Simulations

The atmosphere-ocean coupled model used in this study is the Unified Wave Interface - Coupled Model (UWIN-CM) (Chen et al., 2013; Chen & Curcic, 2016). All simulations use the configuration that was described in Savarin and Chen (2022b) which includes convection-permitting resolution, atmosphere-ocean coupling, and a modification to air-sea flux parameterization to yield a good simulation of the observed MJO event. Simulations are initialized at 00Z on 22 November 2011 and integrated in time for 15 days (360 hours), ending on 7 December 2011.

Briefly, the simulations in this study use the Weather Research and Forecasting (WRF) model v3.6.1 with the Advanced Research (ARW) dynamical core (Skamarock et al., 2008) for the atmosphere component, and the Hybrid Coordinate Ocean Model (HYCOM) v2.2.99 for the ocean (Metzger et al., 2014). The simulated region encompasses the Indian Ocean (IO) and Maritime Continent (MC) with three nested domains of 36-, 12-, and 4 km resolution (Fig. 1a); the outer domains use the Tiedtke convective parameterization (C. Zhang et al., 2011) and the 4-km domain does not use a convective parameterization. HYCOM grid spacing is a uniform  $0.08^\circ$ . Initial and boundary conditions for the simulations come from the European Centre for Medium-Range Weather Forecast (ECMWF) operational forecast fields for the atmosphere (from CR37R2) and daily mean HYCOM global analysis for the ocean (Cummings, 2005; Cummings & Smedstad, 2013). Similar coupled model configurations have been successfully used to model the MJO (e.g., Wang et al., 2021).

The control simulation (CTRL) has real topography over the MC and is configured identically to AO4-FLX in Savarin and Chen (2022b). We then use the same initial and boundary conditions for two idealized simulations in which we modify topography and bathymetry over the MC to different degrees. In the FLAT experiment, MC topography is flattened to a uniform 10 m elevation, and the land-use category for the flattened terrain is changed to evergreen broadleaf forest (Fig. 1b). Using the *metgrid* program provided by the WRF preprocessing system (WPS), atmosphere initial conditions are extended to the surface where topography has been modified, and the ocean initial conditions remain unchanged. In the WATER experiment, MC land is converted to 50 m deep ocean (Fig. 1c). The atmosphere initial conditions are the same as in the FLAT simulation, but the newly created ocean has no currents, while temperature and salinity fields are interpolated from the nearby ocean and smoothed - thus the ocean temperatures, salinities, and SSTs near the MC are smoother than in CTRL and FLAT simulations.

## 2.2 Data

Several observational datasets are used to evaluate the model simulations' performance and to explore the physical processes associated with the MJO and the MC. For precipitation, we use the Integrated Multi-satellitE Retrievals for GPM (IMERG) satellite precipitation estimates (V06B; Huffman, Bolvin, et al., 2019), which are available in half-hourly intervals and at a spatial resolution of  $0.1^\circ$ . 20 years of data (June 2000 - June 2020) are used for MJO tracking and climatology, but when comparing with model simulations, only the 15 days from November 22 - December 7 are considered. In addition to precipitation, we also use the Cross-Calibrated Multi-Platform (CCMP) gridded surface vector winds (V2.0; Atlas et al., 2011), which are available 6-hourly and at  $0.25^\circ$  spatial resolution. To create a distance-from-coastline reference framework for our analysis of the DC over the MC, we use the ETOPO1 dataset, a global relief dataset at a spatial resolution of 1 arcminute (NOAA National Geophysical Data Center, 2009).

## 2.3 Large-scale Precipitation Tracking of the MJO

The large-scale precipitation tracking algorithm (LPT, (Kerns & Chen, 2016, 2020)) is used to track the MJO-associated precipitation in the IMERG dataset. The algorithm tracks a spatially smoothed 3-day precipitation accumulation that exceeds a chosen threshold over an area larger than  $3 \times 10^5 \text{ km}^2$ . Kerns and Chen (2020) use a 12 mm precipitation accumulation threshold on 20 years (1998-2018) TRMM 3B42 data and identify 215 MJO events. Before the application of the algorithm to the IMERG dataset, precipitation data is conservatively re-gridded to  $0.25^\circ$  spatial and 3-hourly temporal resolution to match that of TRMM 3B42. After precipitation is tracked, additional constraints are used to separate MJO events from other large-scale systems, such as a minimum duration of 7 days, and consistent eastward propagation. In the IMERG dataset, the November-December 2011 MJO event remains cohesive and propagates through the MC up to a precipitation threshold of 22 mm. When model simulations are compared to observations, a threshold of 17 mm is used instead of 12 mm to highlight differences between simulations, as the model tends to overproduce precipitation (see Savarin & Chen, 2022b). At lower thresholds, MJO propagation over the MC can be seen in LPT tracking, but it tends to present as a series of discrete longitude jumps, as the tracking algorithm attempts to connect distinct areas of precipitation with little overlap.

## 2.4 Diurnal Cycle Analysis

We analyze the diurnal cycle (DC) relative to its distance from coastline, which can clearly show us the cycling between land and sea breezes in the MC. The method used is illustrated in Fig. 2. We use the 1-arc-minute global relief model dataset, ETOPO1

(Amante & Eakins, 2009) to define a land mask (where global relief is above sea level) and remove islands and bodies of water smaller than  $400 \text{ km}^2$  - the modified land mask is shown in Fig. 2a. Then the Haversine formula is used to calculate great-circle distances from each point to every other point on the globe, and for each point, the distance to its nearest coastline is chosen (Fig. 2a). Negative distances denote inland areas, and positive distances denote areas offshore. In this study, we focus our attention to the western MC ( $90\text{-}120^\circ\text{E}$ ,  $10^\circ\text{S}\text{-}10^\circ\text{N}$ ), and only data from this region are considered whenever the diurnal cycle is analyzed. The number of points in each 25-km distance bin within is MC region is shown in Fig. 2b using a spatial resolution of  $0.1^\circ$  to match the GPM IMERG precipitation dataset.

To construct diurnal cycle composites, precipitation data is first converted to local solar time (LST), which only depends on longitude and is rounded to the nearest hour. The LST offsets inside the MC box range from UTC+6 and  $90^\circ\text{E}$  to UTC+8 at  $120^\circ\text{E}$ . Then precipitation data is binned into 25-km bins for the entire data record and averaged for every LST hour. The resultant distance-from-coastline Hovmöller diagram is shown in Fig. 2c for 20 years (June 2000 - June 2020) of IMERG data, and the diurnal cycle is repeated twice for completeness. Analysis can then be simplified into a more quantitative line diagram in Fig. 2d, where color represents the amount of precipitation at different LST. Displaying the DC in this manner clearly shows the cycling of precipitation between land and ocean (the alternation between land- and sea-breeze) and adds a spatial component to our analysis.

The method described here can be applied to any field, scalar or vector, regardless of whether it is gridded or not. With the additional calculation of bearing based on the Haversine formula, we can obtain the direction from any point to its nearest coastline. This allows us to project vector fields such as surface winds to their across- and along-coastline components with trigonometric functions.

### 3 Diurnal Cycle of Precipitation in MJO and non-MJO Environments

We start by examining the impact of the MJO on the DC of precipitation over the MC in a climatological sense. LPT tracking is used to separate the MC area (outlined in 2a) into two categories: active MJO regions directly inside the convective envelope, and the non-MJO regions outside the convective envelope and its  $5^\circ$  filtering radius. The areas inside the  $5^\circ$  filtering radius between the MJO convective envelope and non-MJO regions are not considered for this analysis. The DC is then composited for each category and shown in Fig. 3, which shows the Hovmöller diagrams of the DC in active MJO and non-MJO environments and their difference (a-c), as well as the more quantitative line diagrams of the DC (e-f), and the average precipitation and the DC amplitude between the two environments (f), all as a function of distance from coastline.

Compared to non-MJO environments, the amount of precipitation is strongly increased during MJO events, which clearly increases the amount of precipitation within the DC. However, the precipitation increase is not uniform throughout the course of the day, nor is it uniform in its position relative to the coastline. The amount of precipitation over water is more than doubled during most of the day, with the greatest increase in the early morning. Precipitation over land shows a generally lesser increase than over water, and it is most prominent in the evening - in the early morning, there are even times when the DC is unaffected by the MJO (Fig. 3c).

These results show that the active MJO increases precipitation over the MC in accordance with the DC but shows a clear preference for amplifying precipitation over water. It rains more where it would already be raining, over land in the afternoon, and over water in the morning, but the water DC is entirely shifted upward, while the land DC is merely amplified. This indicates that the MJO (as defined by precipitation tracking)

is largely carried through the MC over water, and that the DC persists even under large-scale MJO conditions.

#### 4 MJO Characteristics in Model Simulations

To evaluate the relative effects of flattening topography and removing the land and its associated DC over the MC, we consider how the MJO is represented in observations and our simulations. The large-scale precipitation and surface wind fields for the simulations are shown in Fig. 4, Fig. 5 shows time series of precipitation over the MC, Fig. 6 shows the LPT-tracked MJOs. Fig. 7 summarizes some statistics that help characterize the differences in the MJOs among model simulations.

The CTRL simulation does a good job at representing the large-scale environment of the November-December 2011 MJO event (Chen et al., 2016), as can be seen the Hovmöller diagrams of rain rate and surface zonal winds in Fig. 4. The CTRL's precipitation signal is noisier than in observations due to its higher resolution and a high bias in precipitation (see Savarin and Chen (2022b), their AO4-FLX experiment). The post-MJO suppression in CTRL is not as strong as was observed, but it does propagate through the MC, even though the signal is not as smooth as over the IO or in observations (Fig. 4b). The surface westerlies associated with the MJO are well reproduced, and they persist over the IO after the MJO has propagated east. Flattening MC terrain results in small changes in the large-scale environment compared to the CTRL. Over the MC, precipitation seems more scattered and the MJO-associated eastward-propagating precipitation is more difficult to distinguish until 3 December, where a heavy rainfall event forms near 130°E. Surface westerly winds over the MC are stronger than in CTRL, which can be attributed to the removal of topographical barriers. When MC land is removed in the WATER simulation, we see a lot more precipitation and a much clearer eastward propagation associated with MJO convection. After MJO passage, precipitation suppression over the IO is stronger than in previous simulations, as are surface westerly winds - this is a result of reduced friction over the entire MC.

Fig. 5 shows time series of MC precipitation averaged over the MC box outlined in Fig. 2 for IMERG observations and model simulations. All model simulations reproduce an increase in precipitation associated with the MJO that begins after November 25, ahead of the MJO centroid entering the region. The WATER simulation produces the largest amounts of precipitation, and the most precipitation increase associated with the MJO, while simulations containing land produce less of both. This indicates that during MJO passage (the time range during which the MJO centroid is located over the MC are outlined with colored horizontal bars on the bottom of Fig. 5), the presence of MC land is disruptive to MJO-associated precipitation enhancement.

These large-scale differences are reflected in LPT-tracked MJOs shown in Fig. 6. At the 17 mm precipitation threshold, both the CTRL and FLAT simulations dissipate over the MC before the end of the simulation, while the observed and WATER MJOs propagate smoothly. The average 24-hour propagation speed in observations is  $5.8 \text{ m s}^{-1}$ , which is closely matched by  $5.6 \text{ m s}^{-1}$  in WATER. The propagation speeds of CTRL and FLAT MJOs are  $3.4$  and  $3.5 \text{ m s}^{-1}$ , respectively, so in addition to dissipating over the MC, they are also slower.

Soon after the CTRL and FLAT MJOs extend into the MC region (after 28 November), the MJO area begins to shrink, and then remain relatively steady while the MJO centroid is still in the IO. After the MJO centroids enter the MC on 2 December (at which point more than half of the MJO is over the MC), the CTRL and FLAT MJOs begin to quickly dissipate, with the FLAT MJO weakening at a faster rate. The initial reduction in MJO size when first entering the MC is also present in observations - but after the initial weakening, the observed MJO's size remains relatively steady until the end

of the simulation period. As there is no land present in the WATER simulation, the MJO area remains relatively steady throughout the simulation, with some size fluctuations as the tracking algorithm picks up some convection over the western Pacific.

These results show that, as expected, when all obstacles are removed from the MJO's path (such as in WATER), its propagation is smooth, and its precipitation does not weaken. Removing mountains alone but keeping islands where they are (as in FLAT) has a much smaller impact on MJO propagation (compared to CTRL), and, surprisingly, that impact acts to weaken the MJO and impede its propagation even further. In the next section, we take a closer look at the diurnal precipitation patterns over the MC and how they can disrupt MJO propagation to explain this unexpected result.

## 5 Diurnal Cycle of Precipitation

In this section, we examine the DC of precipitation over the MC (90-120°E, 10°S-10°N) for the period from 22 November to 6 December 2011 to evaluate how well the DC is represented in CTRL, and how it changes among model simulations. Fig. 8 shows the average rain rates over all MC land and ocean points (a, b), and the percentage of total rain that falls over them (c) relative to local solar time. To put our 15-day period into broader context, observations for the model period are shown in solid colors and bars, while the dashed lines and hatched bars show the 20-year IMERG climatology. Unsurprisingly, the amount of precipitation in the 15-day period is higher than the 20-year averages at all times of day. This is due to two factors: first, we are considering a shorter period, so extreme rain rates would contribute more strongly to the average, and second, the 15-day model period contains an MJO event, which increases the amount of precipitation over the MC - especially over water (Fig. 3). The signature of the MJO can be inferred from the fact that at any time of day, the portion of precipitation that falls over water is greater in the 15-day composite than in the 20-year one (Fig. 8c). Apart from the difference in magnitude, the 15-day, and the 20-year DC composites over land and water have the same characteristic timing, indicating that the method we use for analyzing the DC is appropriate even for such short time periods.

We noted previously that both the CTRL and FLAT simulations tend to overproduce precipitation (Fig. 4), but when considering only precipitation over the MC ocean points (Fig. 8b), the average rain rates in model simulations accurately reproduce IMERG observations both in intensity and timing of precipitation extrema. In the WATER simulation, the amount of precipitation over water is higher over the course of the day, and closer to the DC we would see over open ocean, with smaller amplitude and a precipitation maximum slightly earlier in the day (Nesbitt & Zipser, 2003). Over MC land, the timing of the diurnal precipitation extrema still matches that of observations, but the precipitation intensity is consistently exaggerated (Fig. 8a), which results in proportionally more rain falling over land. The land-sea contrast present in observations and CTRL and FLAT simulations results in land-locked convection in the afternoon, with convective systems that are much more intense than what we see over water.

The separation of land and water points for the DC of precipitation in Fig. 8 shows that in model simulations, convection over land is more intense than in observations, with a slightly lower-intensity and longer-lasting precipitation peak in FLAT. However, this way of looking at land and sea precipitation obscures the changes in precipitation patterns over land that arise from imposed terrain modifications. To investigate those, Fig. 9 shows distance-from-coastline relative Hovmöller diagrams of rain rate for the 15-day period in observations and CTRL and FLAT simulations (top), and their 15-day composites (bottom). Seen in this manner, we can note that flattening MC terrain results in changes in the location of precipitation, as well as in precipitation frequency.

Compared to observations, the DC of precipitation in CTRL is stronger and more regular, with sea breeze precipitation propagating far inland on most afternoons while observations show more day-to-day variability. As inferred from Fig. 8, the amount of precipitation over land is exaggerated by up to 80% while the amount of precipitation over water is simulated more accurately (Fig. 9e); therefore, the precipitation in the model is more land-dominated than in observations.

Flattening terrain results in precipitation pattern changes that can be separated into two regions over land: the near-coastal region (within 100 km inland), and the far-inland region (more than 200 km inland). In the near-coastal region, the FLAT DC is diminished but remains regular while in the far-inland region, it is strongly amplified in intensity but reduced in frequency. Near the coast, the reduction in peak precipitation is due to two effects - concurrent effects of sea- and valley-breezes that amplify onshore flow in the early afternoon, and mountains near the coast (along the west coast of Sumatra) that both act to amplify precipitation in CTRL but not in FLAT. But the more interesting changes are happening far inland, where sea breezes from different sides of islands (mainly Borneo) in FLAT converge and grow into organized mesoscale convective systems that are more intense, larger, and last longer than in CTRL. Outside of MJO conditions (before 29 November), these systems persist into the next morning and suppress precipitation for the rest of the day, creating a two-day cycle. During active MJO, the increased moisture supply means that these large systems are formed every day. In a 15-day composite from the FLAT simulation (Fig. 9f), inland precipitation peaks are significantly stronger than in CTRL even though they occur less frequently.

To summarize, these results show that model simulations with land-sea contrast simulate the DC over MC water accurately, but show more, and more intense land-locked convection in the afternoon. When terrain is flattened, we see the coastal sea-breeze precipitation is diminished in amplitude, but a convergence of sea-breezes from all around islands, which are no longer disrupted by terrain, results in an amplification of convection far inland. In the next section, we focus on the differences in convective systems that arise from modifying MC terrain.

## 6 Land-Locked Convection and Suppression of MJO Precipitation over Water

In this section, we take a closer look at the differences in land-locked convection between the CTRL and FLAT simulations. As noted previously, the FLAT simulation produces inland convective systems that are more intense, larger, and longer-lasting than in the CTRL simulation (Fig. 9, where mountains disrupt the convergence of sea breezes from different sides of the island. In Fig. 10, we show an example of the evolution of one such convective system in the FLAT simulation that developed overnight between 26 and 27 November. Fig. 11 demonstrates that the case shown in Fig. 10 is not unique, and the associated patterns of low-level convergence and moisture supply are illustrated in Fig. 12.

The evolution of sea-breeze fronts into a large MCS in the FLAT simulation in Fig. 10 shows precipitation and surface wind maps (left) and vertical cross-sections of hydrometeor mixing ratio to indicate clouds (dotted in black), potential temperature anomaly (shaded in color) from the previous hour, and zonal and vertical wind components (right). The vertical cross-sections are plotted with longitude and averaged between 1°S and the equator, and the vertical winds have been multiplied by a factor of 10 for better visibility. The three rows of figures correspond to three different times, one in the early stage of MCS development (21-22 LST on 26 November), when convection is beginning to converge inland, along the south-east coast of Borneo (top), one in the mature stage (00-01 LST on 27 November) when convection is organized on a very large scale (middle), and one in the dissipating stage (05-06 LST on 27 November), when convection is dis-

400 sipating in this region, but intense precipitation has migrated to the north and west (bot-  
 401 tom).

402 The evolution of the convective system in Fig. 10 indicates that in the FLAT sim-  
 403 ulation, a large, organized, and robust mesoscale convective system (MCS) and its as-  
 404 sociated circulation develop and propagate over Borneo. During the early stage, the sys-  
 405 tem is just beginning to propagate and develop inside the averaging box near 115°E (Fig.  
 406 10a). There is some upward motion, and a weak warm anomaly is beginning to develop  
 407 in the mid-troposphere, coincident with where clouds are present (Fig. 10d). Three hours  
 408 later, the system has matured and is more than 200 km across, with strong updrafts and  
 409 strong mid- and upper-tropospheric heating, indicating that the MCS is beginning to  
 410 develop its own circulation and a broad upper-level region of stratiform clouds (Fig. 10b,  
 411 e). The presence of a deep inflow layer we can see in Fig. 10e is associated with mature  
 412 MCSs, where large regions of stratiform clouds and precipitation are likely present, and  
 413 has been numerically shown by Mechem et al. (2002). Five hours later, the system has  
 414 grown to over 300 km across and precipitation is dissipating inside the averaging box as  
 415 the system is propagating away from it. There is subsidence from the mid-troposphere,  
 416 and warming has moved closer to the surface, while upper levels begin to cool (Fig. 10c,  
 417 f).

418 To show that the development of the MCS described in Fig. 10 is not a singular  
 419 occurrence but a systematic difference between CTRL and flat simulations, we take the  
 420 five most intense convective events that occur far inland and compare the results between  
 421 the simulations. The five most intense events are determined based on average rainfall  
 422 rate more than 200 km inland and marked with stars next to the Hovmöller diagrams  
 423 in Fig. 9. Fig. 11 shows the time series of far-inland rain rate (top), with the highlighted  
 424 intense convective events and the rain rate thresholds that need to be exceeded for each  
 425 simulation. The thresholds have been chosen so that they result in the same number of  
 426 hours within the simulation during which the threshold is exceeded. A rain rate thresh-  
 427 old of 3.6 mm hr<sup>-1</sup> in FLAT results in 20 hours separated between 5 convective events,  
 428 while the same number of hours and convective events are identified with a threshold of  
 429 2.2 mm hr<sup>-1</sup> in CTRL - the convective events are over 60% more intense in FLAT. The  
 430 precipitation for the highlighted times is composited together for the CTRL and FLAT  
 431 simulations (Fig. 11b, c), and their difference is shown in Fig. 11d, with red colors in-  
 432 dicated where rain rates are higher in FLAT than in CTRL.

433 Large land-locked convective events in the FLAT simulation are spread over larger  
 434 and more central areas of islands, and that the precipitation that occurs in them is more  
 435 intense when compared to the systems that develop in CTRL. These large MCSs sup-  
 436 press precipitation over the surrounding waters (brown shading in Fig. 10) where the  
 437 MJO is attempting to enhance precipitation around the same time of day. In FLAT, the  
 438 larger and more intense MCSs can develop because there is no terrain disrupting the con-  
 439 vergence of sea breezes from different sides of the islands, and there are no mountains  
 440 forcing upward motion in specific locations.

441 The systematic differences in precipitation patterns between CTRL and FLAT are  
 442 also evident in the accompanying patterns of low-level convergence and water vapor sup-  
 443 ply shown in Fig. 12. The compositing is done in the same manner as for precipitation  
 444 in Fig. 11, and we can see that most of Borneo is covered in large-scale convergence in  
 445 the FLAT simulation (Fig. 12c). In CTRL, the convergence region is smaller and less  
 446 contiguous, and we also see the signature pattern of elevated topography, with dipoles  
 447 of convergence and divergence in the north of the island (Fig. 12a). The convergence and  
 448 water vapor mixing ratio shown are averages for a layer that spans between 1000 and  
 449 700 hPa, indicating that the low-level convergence is not confined solely to the bound-  
 450 ary layer, which implies a presence of mature MCSs and elevated mid-level moisture (Mechem  
 451 et al., 2002). But the sharper difference is evident when looking at low-level moisture  
 452 availability - due to elevated terrain in CTRL, large areas of Borneo show much lower

water vapor content near the surface than in FLAT (Fig. 12b, d). In fact, the during the most intense convective events, low-level convergence in FLAT is 58% higher than in CTRL, and the low-level water vapor shows a 3% increase, indicating that convection mainly grows due to increased and widespread convergence. Fig. 12 explains why convective systems can grow larger and stronger in FLAT in a physical sense - the collocation of low-level convergence and moisture supply can support precipitation. In CTRL, though we see large areas of convergence, the moisture supply is lower, so the systems can only grow in a limited capacity.

These effects can be seen in the differences between the composite DC in the CTRL and FLAT simulations separated into the MJO and non-MJO environments shown in Fig. 13, following the same method as in Section 3. We can clearly see the amplified enhancement of far-inland convection in the early morning on the FLAT simulation, while far-inland convection is slightly suppressed by the MJO in CTRL. At the same time, the enhancement of precipitation over water in MJO environments is smaller in FLAT than in CTRL, indicating that the mountains in CTRL present a physical barrier to MJO flow, but they also disrupt the large-scale organization of convection due to convergence of multiple sea breeze fronts. The resulting MCSs that develop over land in CTRL occur on a smaller scale - which is still disruptive to the MJO, but to a lesser extent. So, in a way, mountains can help the MJO propagate across the MC by disrupting the large convective systems that would develop in their absence.

## 7 Summary and Conclusions

This study investigates the MC barrier effects to MJO propagation through a systematic analysis of the impacts of MC terrain and land-sea contrast. Three atmosphere-ocean coupled simulations at convection-permitting resolution are conducted to evaluate the responses in MJO evolution and eastward propagation to changes in MC topography.

The main results can be summarized as follows:

1. Land and land-sea contrast weaken the MJO and disrupt its propagation over the Maritime Continent.
2. Land-sea contrast of MC islands induces a strong diurnal cycle with strong land-locked convection in the afternoon.
3. Mountains are less disruptive to MJO propagation than the larger and stronger land-locked convective systems that form over land without them.

When MC land is removed and replaced by shallow ocean (the WATER simulation), the MJO moves across the region as a smoothly-propagating, coherent area of large-scale precipitation that does not weaken in the process. When islands are present, with or without mountainous terrain, the MJOs over the MC are first reduced in area, and eventually dissipate over the region. This indicates that the presence of land and the land-sea contrast induced by it act to weaken the MJO during its propagation over the region (Figs. 4, 6, 7). This was an expected result, and it agrees with previous studies showing that once an MJO enters the MC, it is frequently weakened, and its structure altered by land interactions (e.g., Burleyson et al., 2018; Hagos et al., 2016; C. Zhang & Ling, 2017).

As land is introduced into the MC without terrain (FLAT simulation), it results in the addition of a DC that follows the pattern of the coastal regime described in Kikuchi and Wang (2008). This regime experiences an alternating diurnal pattern characterized by offshore phase propagation with peak precipitation occurring in late evening and early morning (the land breeze; Fig. 8b), and onshore phase propagation with more intense peak precipitation in the afternoon (the sea breeze; Fig. 8a). The resulting convective

systems over land can be separated into two types. The near-coastal convection that is directly forced by sea-breezes (and the background flow) is present on each day of the model simulation. The far-inland convection that is forced by the convergence of multiple sea breezes (and the background flow) is present on each day during active MJO conditions, but only occurs every other day before MJO arrival (Fig. 9c). The far-inland sea breeze convergence results in the formation of very large organized MCSs that develop their own circulation, produce heavy-precipitation, and last well into the morning hours (Figs. 9c, 10). The long-lasting systems then suppress the far-inland convection on the following day (when there is no MJO) due to reductions in mid-upper-level moisture and insolation-induced surface heating. During active MJO conditions, the intense far-inland MCSs are triggered every day due to increased background moisture and upward vertical velocity.

The large daily MCSs that form far inland in the FLAT simulation last into the next morning, suppressing precipitation that is supposed to be initiating over coastal waters at the same time due to the land breeze. The early morning is also the time during which, climatologically, the MJO tends to most enhance precipitation over water, and this local suppression works against that. Therefore, the large land-locked MCSs that develop in the later afternoon and persist until morning reduce the precipitation enhancement over water that happens due to the MJO (Fig. 13c) and result in a weakened MJO with a discontinuous propagation across the MC (Figs. 6c, 7).

The mountainous terrain added in CTRL provides a disruption to the FLAT DC that results in a change in diurnal precipitation patterns. Compared to FLAT, the amount of precipitation falling over land is increased in CTRL (Fig. 8a), but it is distributed in smaller systems that are less disruptive to the MJO. The amplitude of the DC near the coastline, both of land and water) is increased (Fig. 9e) while the systems that develop far inland are smaller in area and less intense (Fig. 11). The low-level convergence associated with these systems is much weaker than in FLAT due to flow disruption by mountains, and as they cannot grow as large, they induce less suppression to precipitation developing over nearby waters (Figs. 12, 13a, b).

Compared to FLAT, the MJO propagation in CTRL is smoother contains more precipitation, and dissipates later (Figs. 6b, 7). This implies that considering that the land-sea contrast is disruptive to the MJO, mountains act to reduce the disruption to MJO propagation, because they disrupt the even-stronger MCSs that would develop in their absence.

## 8 Discussion

Our results show that the active MJO in IMERG observations increases the amount of precipitation throughout the MC, and thus increases the amplitude of the DC over both land and water (Fig. 3), though the increase over water is dominant. These results disagree with previous studies on the subject, which found that while the amplitude of the DC over water is increased by an active MJO, the amount of precipitation over land is reduced (Oh et al., 2012; Rauniyar & Walsh, 2011). We believe the reason for this discrepancy lies in the methodology of MJO and DC identification. Most other studies of the MJO identify events based on the Real-Time Multivariate MJO Index (RMM, Wheeler & Hendon, 2004), or similar indices based on global anomaly fields. Our MJO identification method relies on large-scale precipitation tracking (LPT), which directly tracks MJO precipitation, and only considers the points that lie inside the MJO convective envelope as active, so that at any one time, parts of the MC can be inside the MJO, while other parts are not.

Our results also disagree with the earlier study by (Inness & Slingo, 2006) which finds that it is the mountains, and not the presence of islands, that blocks MJO prop-

agation through the MC. However, their model simulations were performed at very low resolution ( $2.5^\circ \times 3.75^\circ$ ), and many studies have shown that increasing resolution helps with the representation of the MJO (Love et al., 2011; Savarin & Chen, 2022a), so their findings could be attributed to something other than the barrier effect of the MC.

A similar set of convection-permitting simulations with real and flattened topography was performed by H. Tan et al. (2022) and by Zhou et al. (2021), both without dynamic atmosphere-ocean coupling and for two different MJO events. H. Tan et al. (2022) find similar high biases in the DC of land precipitation that are characteristic of our simulations, but also show a low bias in the amplitude of the DC over water, indicating that air-sea coupling could be an important contributor to the variability of precipitation over water. Their results generally agree with our study in that when topography is removed, the peak precipitation over land is reduced, but tapers off more slowly than when topography is present (e.g., Fig. 8a). Though their analysis focuses on different aspects of the DC, the fact that they find similar differences in their simulations makes the results of our study more robust.

We recognize that the afternoon peak land-locked convection in our coupled model simulations is higher than indicated by IMERG observations (Fig. 8a), though it is unclear whether the land precipitation bias is as large as it appears. Previous studies have found the resolution of IMERG to be high enough to accurately represent the DC of precipitation (e.g., J. Tan et al., 2019), and our results qualitatively compare well with precipitation radar studies in the region from the TRMM era (e.g., Biasutti et al., 2012). But the accuracy of hourly IMERG precipitation retrievals over the MC region’s sharp land-sea contrast areas and dynamic terrain has not yet been thoroughly evaluated. Some evaluation studies indicate that IMERG tends to underestimate precipitation associated with tropical cyclone precipitation over the United States (e.g., Mazza & Chen, 2022; F. Tian et al., 2018), while a study by Hayden and Liu (2021) showed both regional under- and over-estimates in the tropics. In addition, many modeling studies performed at higher resolutions show a high bias in land convection over the MC; at lower resolutions, the timing of the DC as well as its amplitude are frequently misrepresented (e.g., Love et al., 2011; Watters et al., 2021).

Though this study only contains model simulations of a single (though well-observed) MJO event, our findings have large implications for numerical modeling of the MJO and its propagation over the MC. Specifically, we expose the role of mountainous and diverse terrain over the MC as important to disrupting the formation of very large MCSs over land that could act to obstruct MJO propagation. In models run with low-resolution terrain (such as in climate simulations), MC mountains would appear smoother and flatter, and their effects on the DC would be smaller. Based on the results of this study, they would provide a lesser disruption to the formation of large land-locked MCSs, and, consequently, they would provide a greater barrier to MJO propagation over the MC.

## Open Research

The datasets used in this study include the high-resolution global terrain model (ETOPO1; NOAA National Geophysical Data Center, 2009), the Global Precipitation Measurement’s Integrated Multi-satellite Retrievals (IMERG; Huffman, Stocker, et al., 2019), and the Cross-calibrated Multi-platform gridded surface vector winds (CCMP; Wentz et al., 2015). UWIN-CM (the Unified Wave Interface - Coupled Model) was used to run the simulations, and is described in Section 2.1 as well as in previous studies such as Savarin and Chen (2022b). The modeling software is available upon request. The large-scale precipitation tracking algorithm for MJO identification is available at <https://github.com/brandonwkerns/lpt-python-public.git>. Data processing and visualization were done in Python v3.6.

## Acknowledgments

The authors would like to thank Brandon Kerns for his help and insight with UWIN-CM model simulations and help with the LPT tracking algorithm used for identifying MJO events. This study was supported by research grants from NOAA CVP (NA15OAR4320063) and the first author was supported in part by the NASA Earth and Space Science Fellowship (NESSF 80NSSC17K0748).

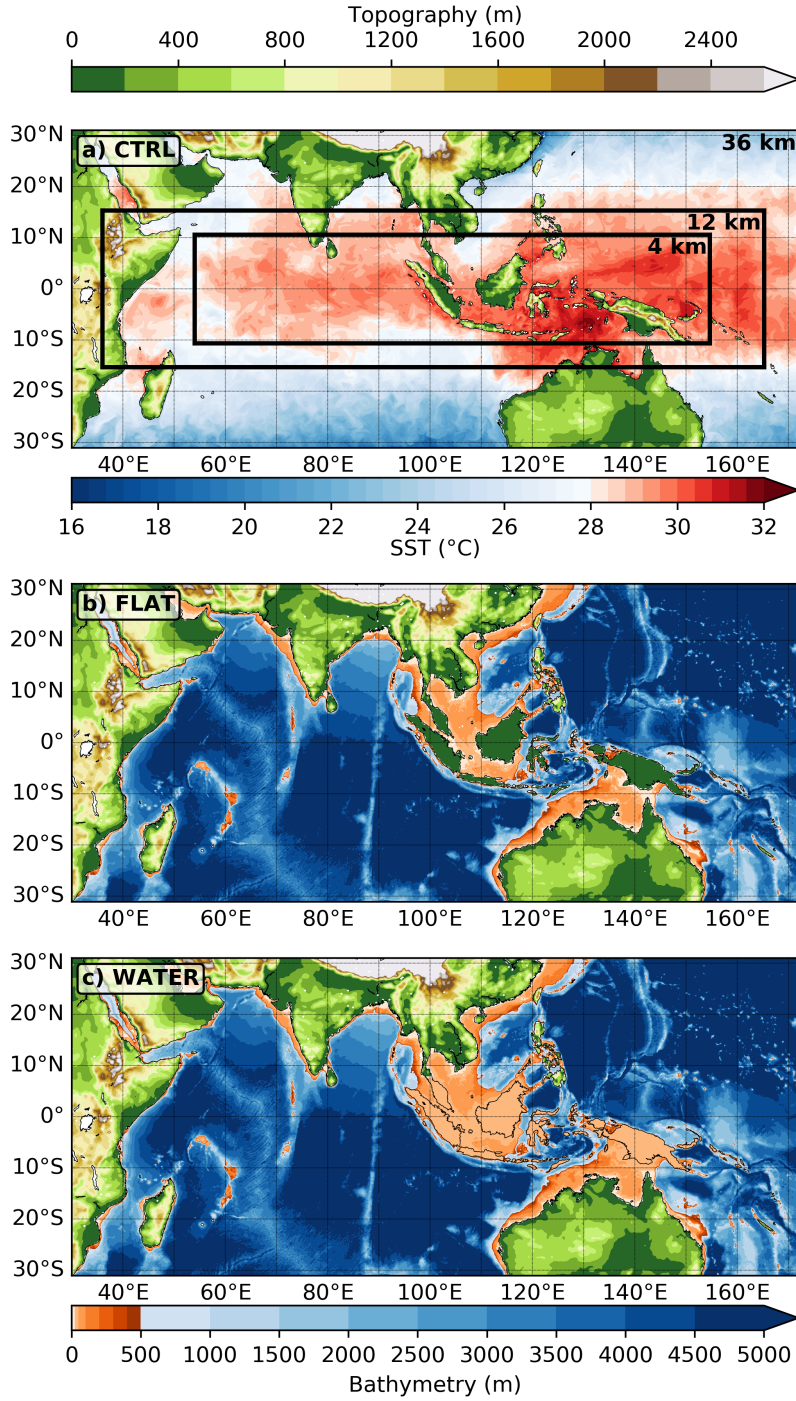


**Figure 1.** Domain configuration and relief in model simulations. a) CTRL topography (m) and initial time SST (°C); b) FLAT topography and bathymetry (m); and c) WATER topography and bathymetry (m). Black rectangles in a) show the boundaries of nested domains the atmosphere.

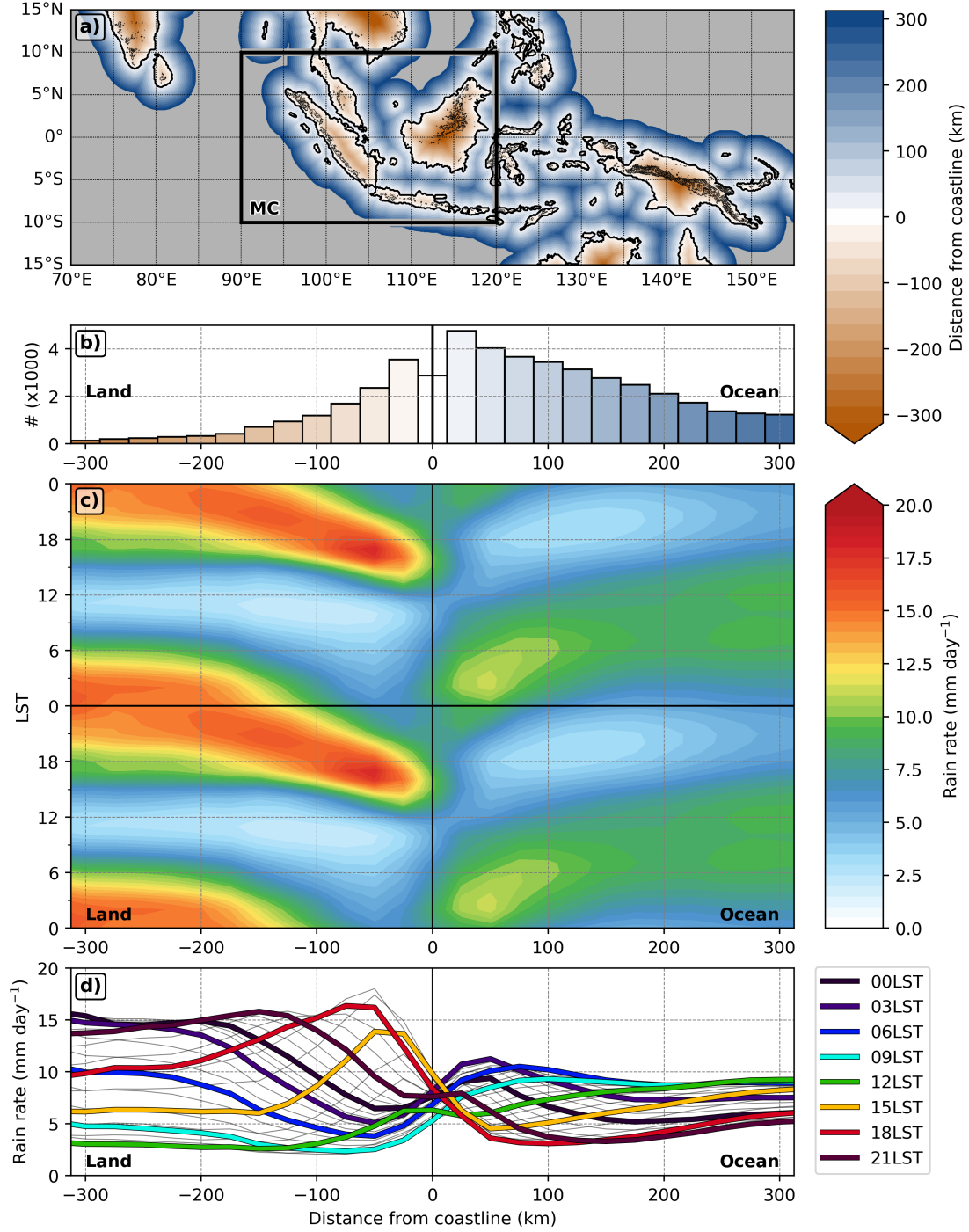


**Figure 2.** Illustration of DC analysis. a) Distance from coastline over the MC (km, negative distances are over land), with the outlined MC area where the DC is analyzed; b) number of points in each 25-km distance bin inside the MC box; c) distance from coastline Hovmöller composite of 2000-2020 IMERG rain rate DC (mm day<sup>-1</sup>), repeated twice; d) quantitative composite of the IMERG rain rate DC (mm day<sup>-1</sup>), with color representing LST.

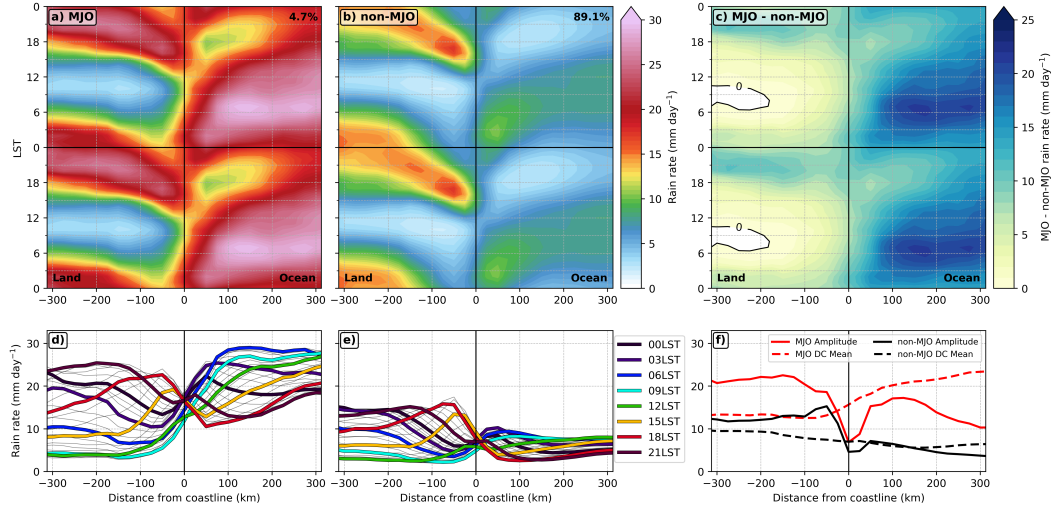


**Figure 3.** 20-year IMERG DC composites in a, d) MJO and b, e) non-MJO environments and c, f) MJO - non-MJO DC composite differences. The color bar in a) and b) is the same as in 2c up to  $20 \text{ mm day}^{-1}$  for easy comparison, and new colors have been added for rain rates above  $20 \text{ mm day}^{-1}$ . In f), the solid lines show the amplitude of the DC composite, and the dashed lines show the average value of the DC composite, red for areas inside the MJO convective envelope, and black for areas outside the envelope and its  $5^\circ$  filtering area. The percentages of in the top right corner of a) and b) denote the percentage of time that the MC experiences MJO and non-MJO environments, respectively. The remaining 6% is the area outside the MJO but inside the  $5^\circ$  filtering area.

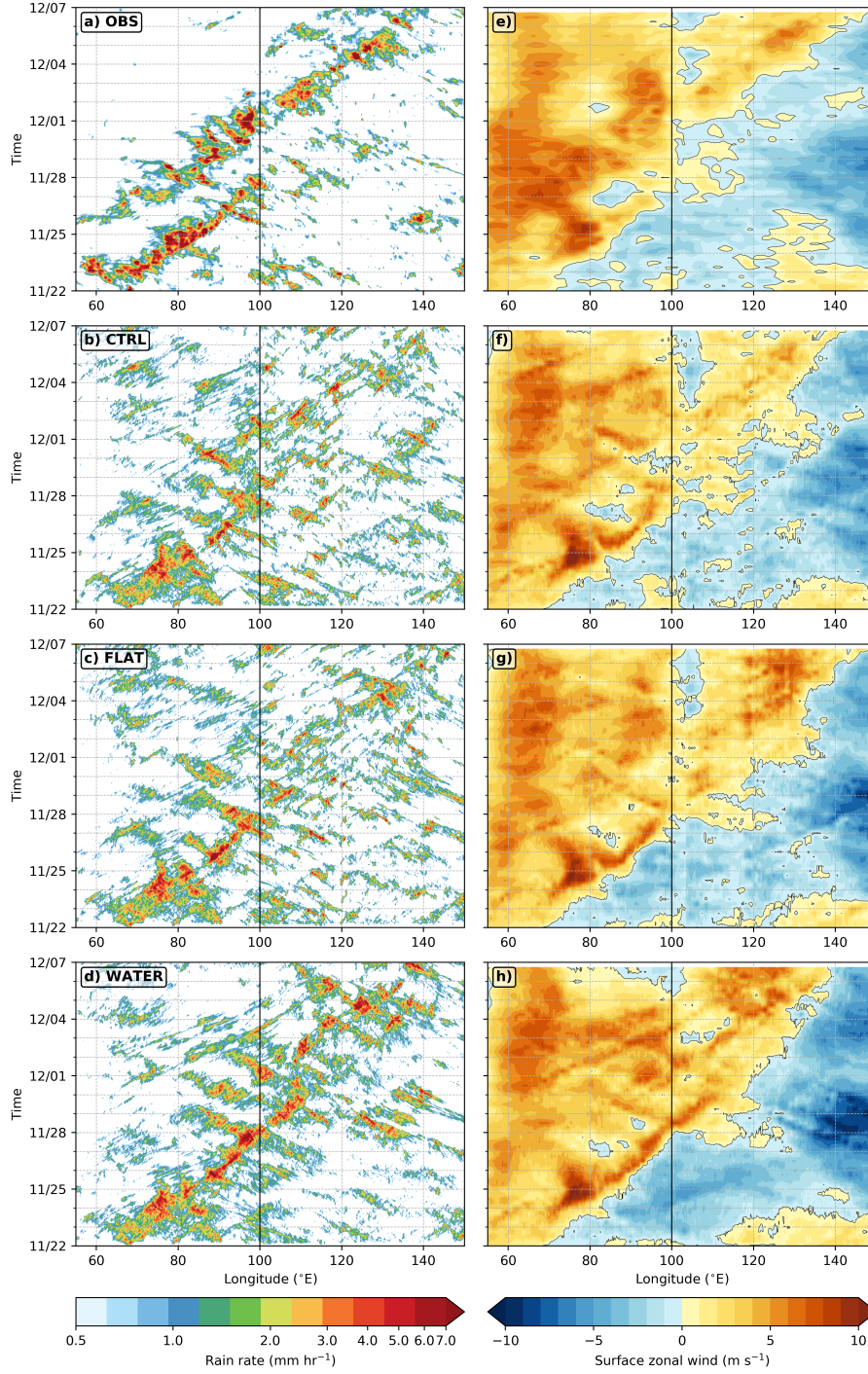


**Figure 4.**  $5^{\circ}\text{S} - 5^{\circ}\text{N}$  Hovmöller diagrams of rain rate (left,  $\text{mm hr}^{-1}$ ) and surface zonal wind (right,  $\text{m s}^{-1}$ ) in observations and model simulations. The products are ordered from top to bottom as follows: observations (IMERG precipitation and CCMP surface winds), CTRL, FLAT, and WATER simulations. The vertical line at  $100^{\circ}\text{E}$  denotes the separation of the IO and MC. CTRL simulation contains real topography, which is flattened over the MC in FLAT, and completely removed in WATER experiments.

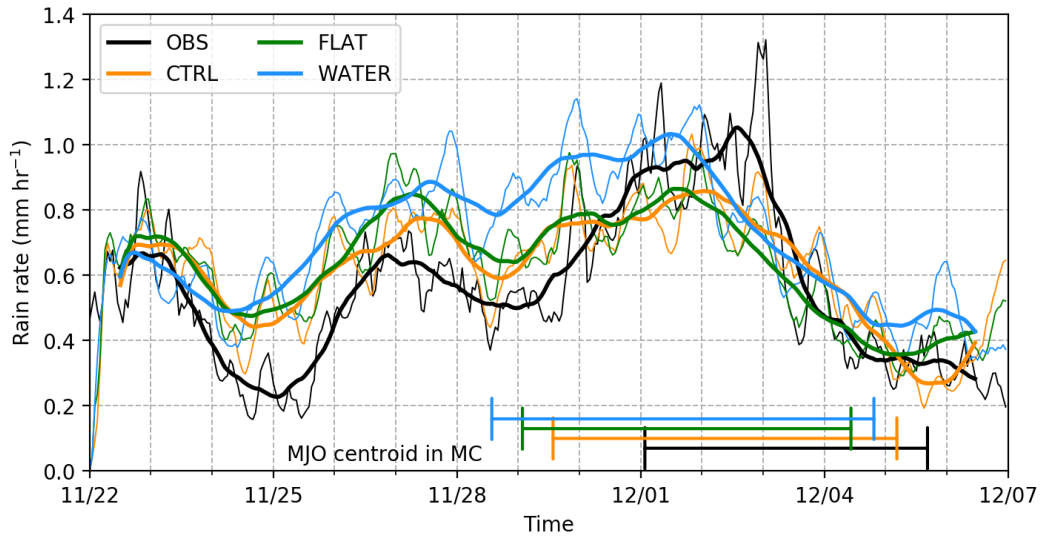


**Figure 5.** Time series of average rain rates over the MC (90-120°E, 10°S-10°N). Thick lines show the 24-hour running mean of hourly precipitation. The horizontal bars indicate the time during which the MJO centroid is over the MC. Observations are from IMERG; CTRL simulation (orange) contains real topography, which is flattened over the MC in FLAT (green), and completely removed in WATER experiments (blue).

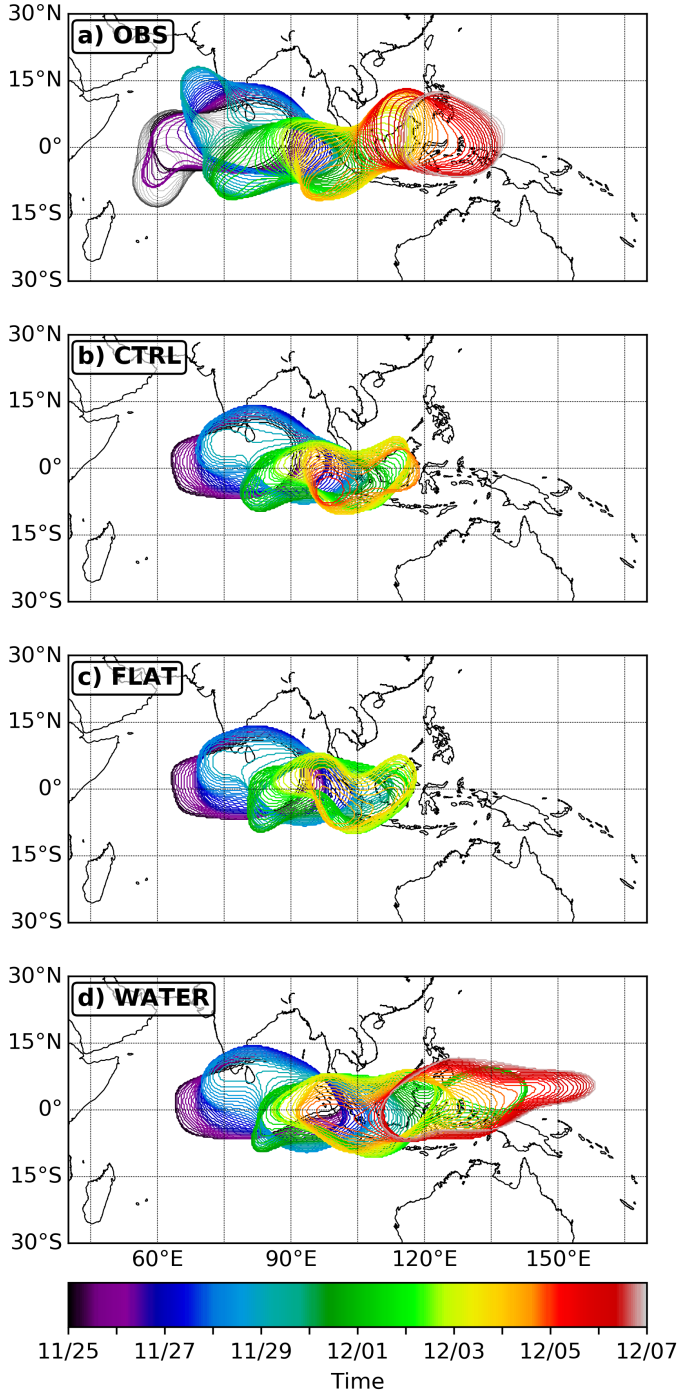


**Figure 6.** LPT tracking of the MJO convective envelope in a) IMERG observations, b) CTRL, c) FLAT, and d) WATER simulations at the 17 mm precipitation accumulation threshold. The colors represent the MJO convective area at a given time. CTRL simulation contains real topography, which is flattened over the MC in FLAT, and completely removed in WATER experiments. Observations (black) are from tracking IMERG precipitation at a 17 mm threshold. CTRL simulation contains real topography, which is flattened over the MC in FLAT, and completely removed in WATER experiments.

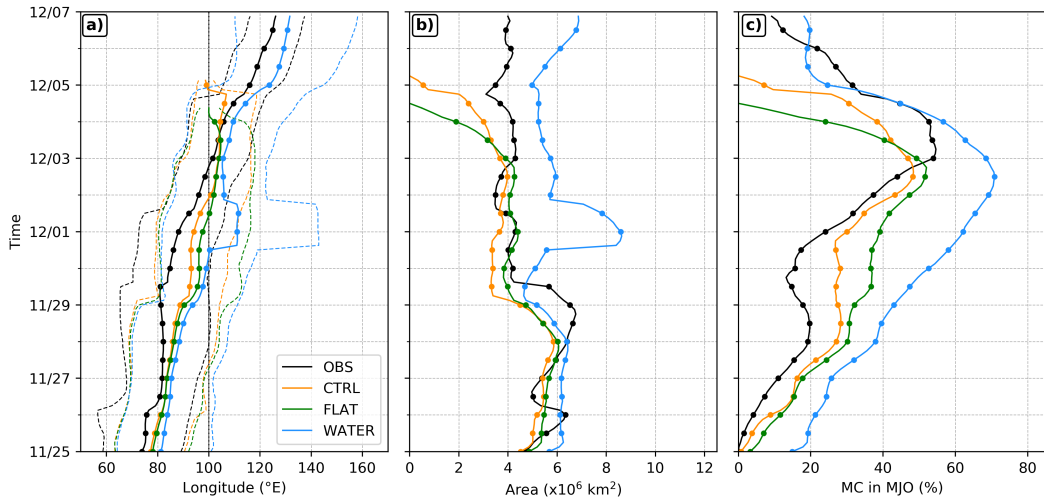


**Figure 7.** MJO tracking summary with time. a) Location of the MJO centroid (solid lines) and its trailing and leading edges (dashed lines), b) MJO area ( $\times 10^6$  km<sup>2</sup>), and c) the portion of MC inside the MJO (%). The MC area is defined from 90-120°E, 10°S-10°N as in Fig. 2a. The vertical line at 100°E in a) denotes the separation between the IO and MC. Observations are from IMERG; CTRL simulation (orange) contains real topography, which is flattened over the MC in FLAT (green), and completely removed in WATER experiments (blue).

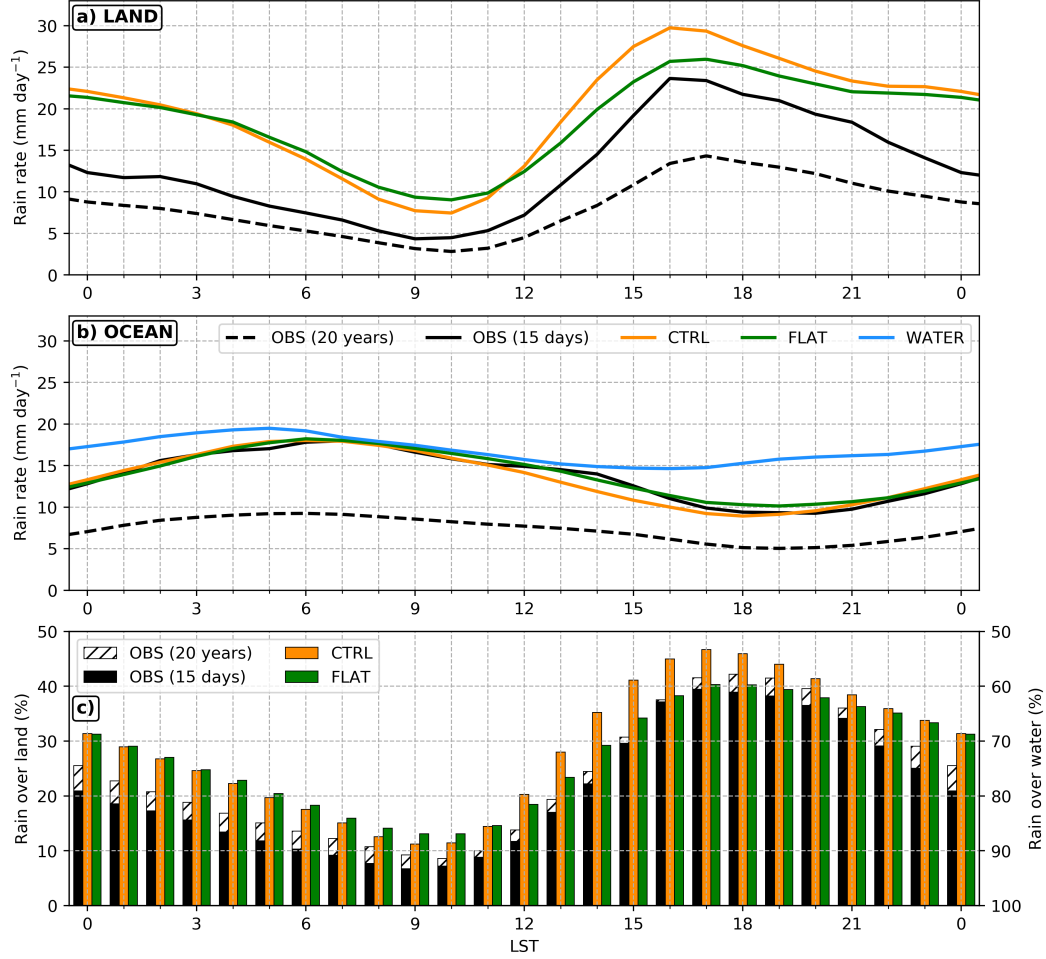


**Figure 8.** DC of precipitation over the MC. The DC is shown over a) land points and b) ocean points; c) percentage of total precipitation over the MC that falls over land (left axis), or water (right axis). The dashed black lines show the 20-year composite DC, while the solid black lines are only for the period of the model simulation. The DC is only composited over the MC area outlined in 2a. Observations are from IMERG; CTRL simulation (orange) contains real topography, which is flattened over the MC in FLAT (green), and completely removed in WATER experiments (blue).

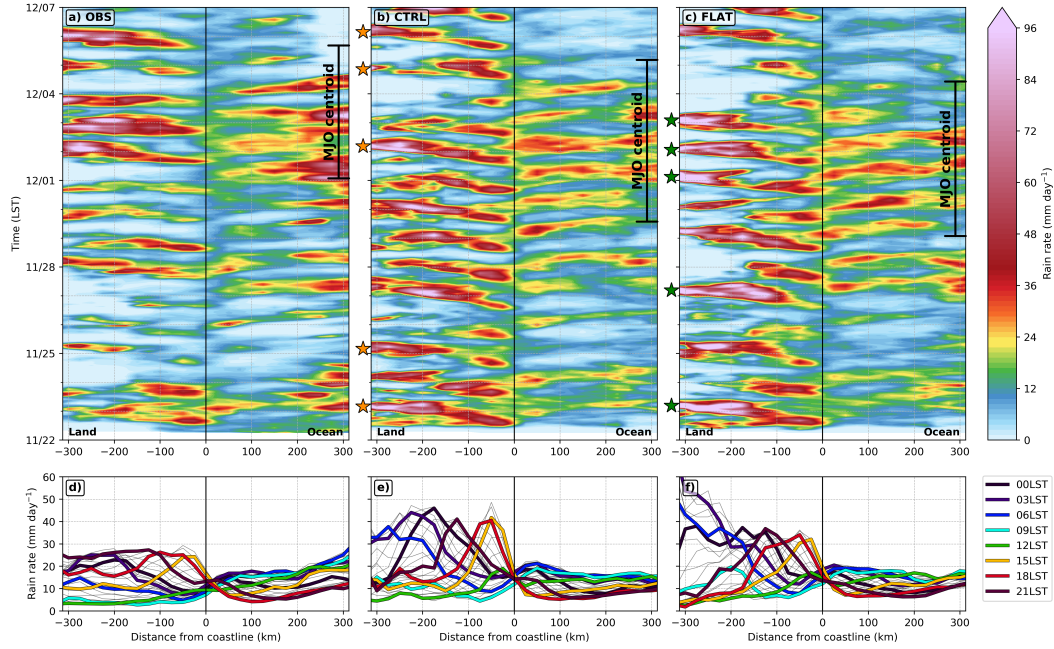


**Figure 9.** Distance-from-coastline DC composites. Top: hovmöller diagrams of rain rate ( $\text{mm day}^{-1}$ ) with LST for a) IMERG observations, b) CTRL, and c) FLAT simulations. Bottom: quantitative 15-day composite DC of rain rate ( $\text{mm day}^{-1}$ ) for d) IMERG observations, e) CTRL, and f) FLAT simulations. The arrows on the right edge of Hovmöller diagrams denote the times during which the MJO centroid is located over the MC (between  $90$  and  $120^\circ\text{E}$ ). The stars on the left indicate the five most intense convective events that occurred more than  $200$  km inland (see Fig. 11). Observations are from IMERG; CTRL simulation contains real topography, which is flattened over the MC in the FLAT experiment.

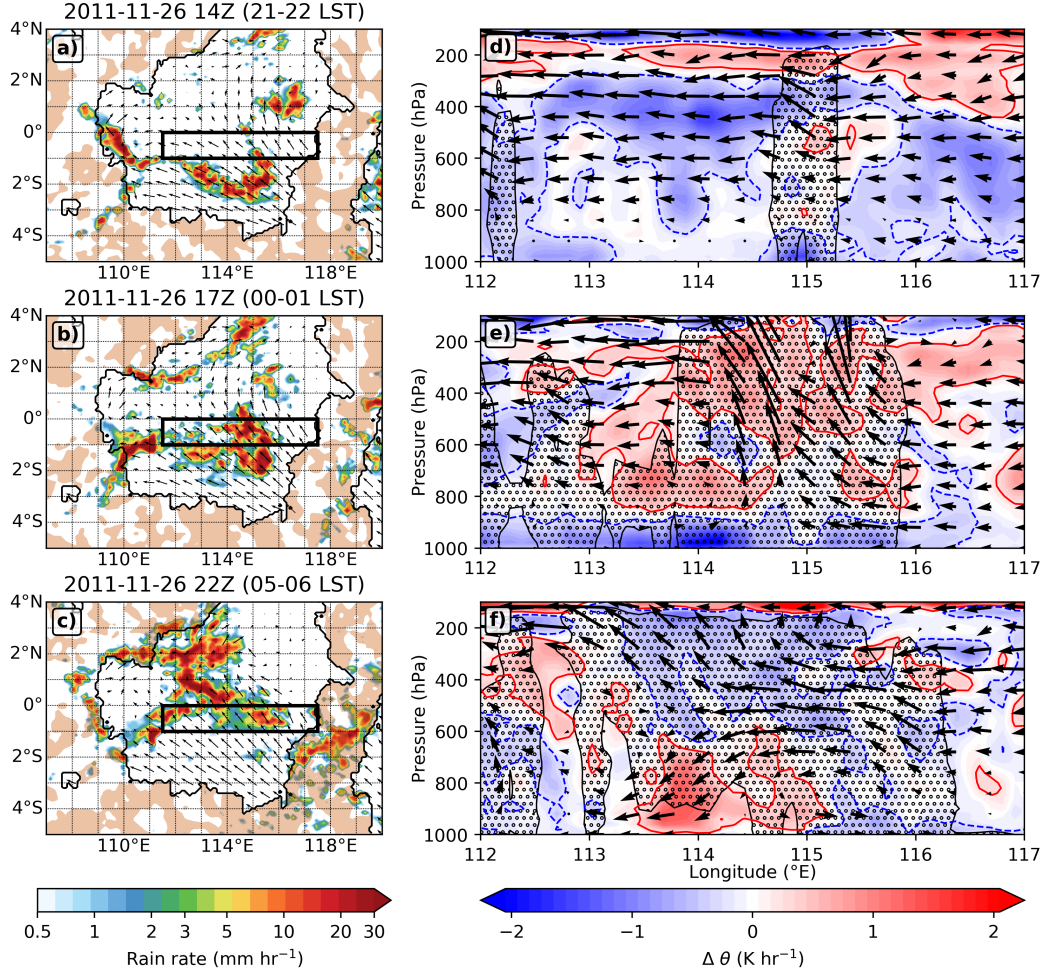


**Figure 10.** Evolution of a large, long-lasting mesoscale convective system in the FLAT simulation (flattened topography over the MC). Left: 3-hourly averaged precipitation ( $\text{mm hr}^{-1}$ ), 10 m winds over land (vectors), and 500 hPa downward vertical velocity over water (brown shading) centered on 26 November at a) 14Z (21-22 LST), b) 17Z (00-01 LST on Nov 27), and c) 22Z (05-06 LST on Nov 27). Right:  $1^{\circ}\text{S}$ - $0^{\circ}$  averaged vertical cross-sections of zonal and vertical winds (arrows), potential temperature change from the previous hour ( $\text{K hr}^{-1}$ ; red-blue shading), and cloud area approximated by hydrometeor content (black hatching) for the corresponding times. Vertical velocity is multiplied by 10 to emphasize the pattern, and red and blue contours outline a temperature change of  $0.25 \text{ K hr}^{-1}$ .

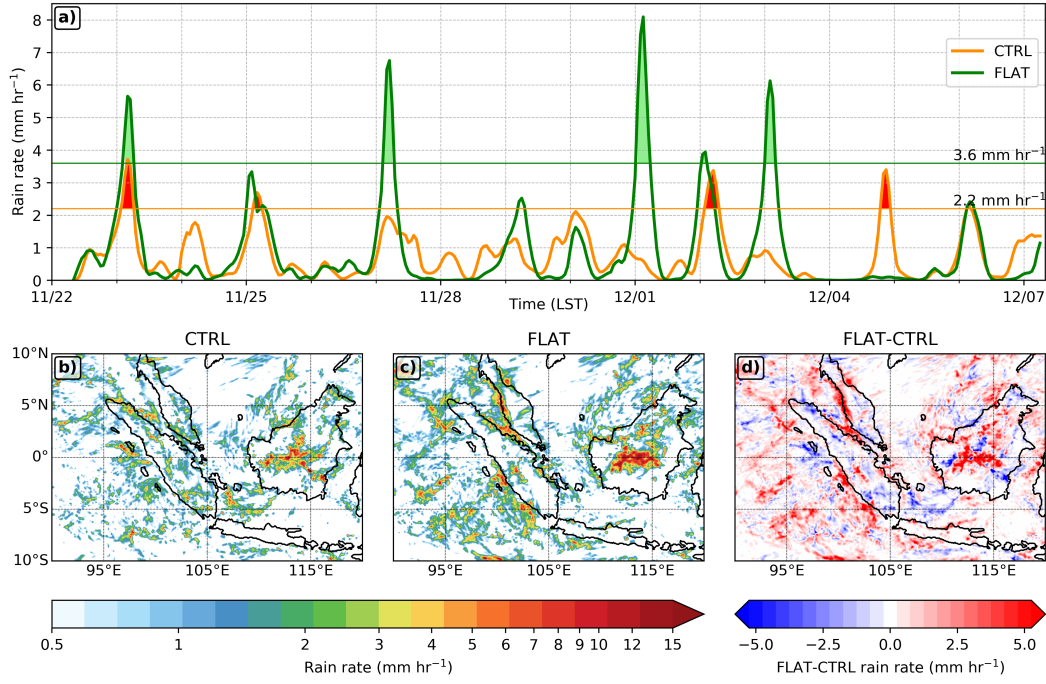


**Figure 11.** Comparison of inland convective systems in CTRL and FLAT simulations. a) Time series (in LST) of rain rate ( $\text{mm hr}^{-1}$ ) averaged over land areas greater than 200 km from the coast, highlighting the five most intense convective events for each simulation. b, c) Rain rate ( $\text{mm hr}^{-1}$ ) composites of the five intense convective events in CTRL and FLAT simulations, respectively. d) The difference in precipitation ( $\text{mm hr}^{-1}$ ) associated with intense convective events between FLAT and CTRL simulations. CTRL contains real topography, while in FLAT, topography over the MC is flattened to sea level.

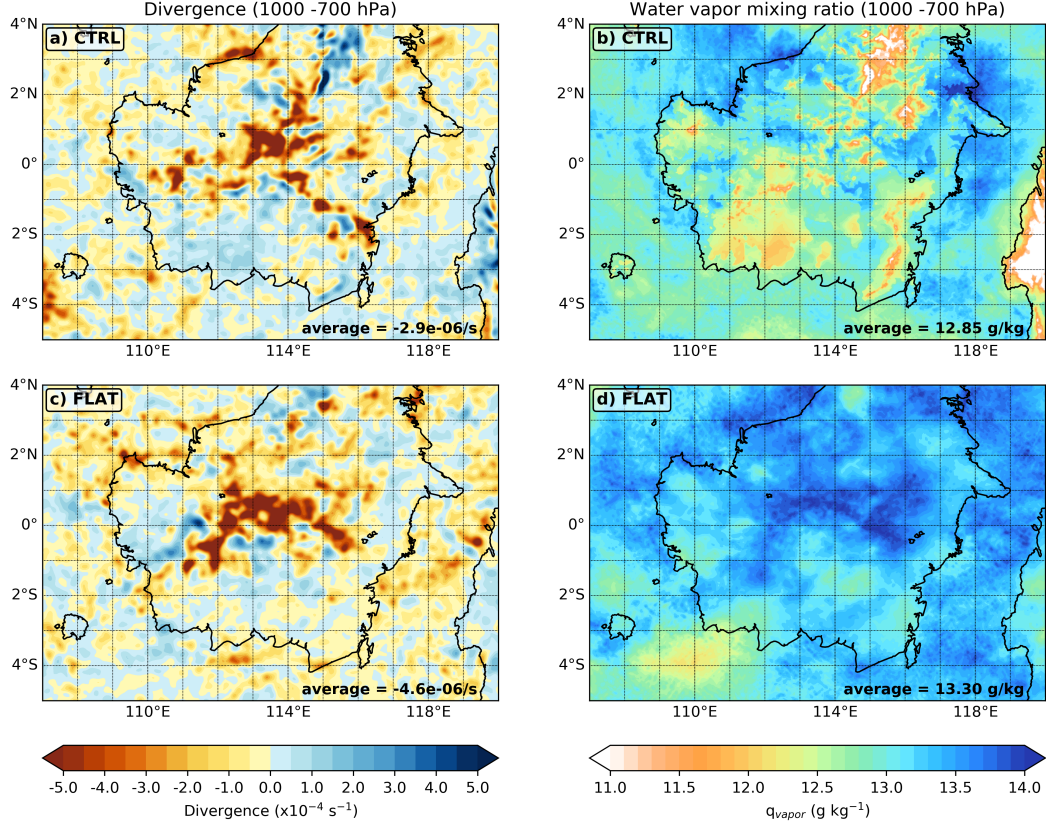


**Figure 12.** Comparison of 1000-700 hPa divergence ( $\text{s}^{-1}$ , left) and water vapor mixing ratio ( $\text{g kg}^{-1}$ , right) in the CTRL (top) and FLAT (bottom) simulations. The comparison is made using the five most intense convective events for each simulation, as defined in Fig. 11. The numbers at the bottom right indicate regional averages of the depicted fields. CTRL contains real topography, while in FLAT, topography over the MC is flattened to sea level.

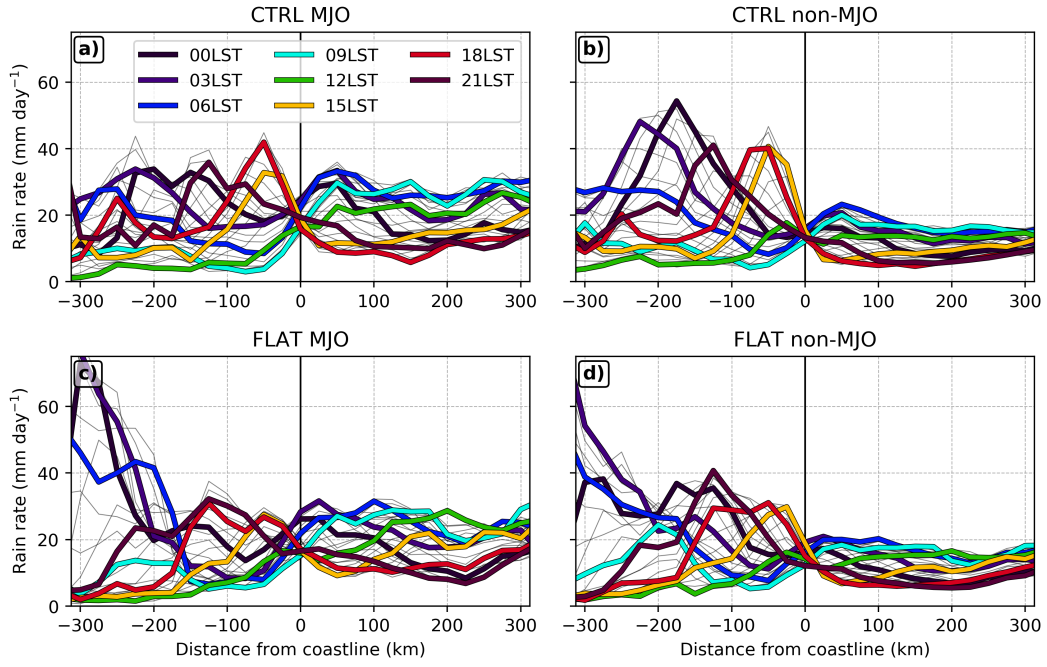


**Figure 13.** Comparison of DC composites for the CTRL (real topography, top) and FLAT (flattened topography over the MC, bottom) simulations under MJO (left) and non-MJO environments (right). The MJO and non-MJO environments are defined as in Section 3 and Fig. 3.

## References

- Abbs, D. J., & Physick, W. L. (1992). Sea-breeze observations and modelling: review. *Australian Meteorological Magazine*, 41, 7-19.
- Amante, C., & Eakins, B. W. (2009, March). *ETOPO1 1 arc-minute global relief model: procedures, data sources and analysis* (Tech. Rep. No. NGDC-24). Boulder, CO, USA: National Geophysical Data Center. doi: <https://doi.org/10.7289/V5C8276M>
- Atlas, R., Hoffman, R. N., Ardizzone, J., Leidner, S. M., Jusem, J. C., Smith, D. K., & Gombos, D. (2011). A cross-calibrated, multiplatform ocean surface wind velocity product for meteorological and oceanographic applications. *Bulletin of the American Meteorological Society*, 92, 157-174. doi: <https://doi.org/10.1175/2010BAMS2946.1>
- Biasutti, M., Yuter, S. E., Burleyson, C. D., & Sobel, A. H. (2012). Very high resolution rainfall patterns measured by TRMM precipitation radar: Seasonal and diurnal cycles. *Climate Dynamics*, 39, 239-258. doi: <https://doi.org/10.1007/s00382-011-1146-6>
- Birch, C. E., Webster, S., Peatman, S. C., Parker, D. J., Matthews, A. J., Li, Y., & Hassim, M. E. E. (2016). Scale interactions between the MJO and the Western Maritime Continent. *Journal of Climate*, 29(7), 2471 - 2492. doi: <https://doi.org/10.1175/JCLI-D-15-0557.1>
- Burleyson, C. D., Hagos, S. M., Feng, Z., Kerns, B. W. J., & Kim, D. (2018). Large-scale environmental characteristics of MJOs that strengthen and weaken over the Maritime Continent. *Journal of Climate*, 31(14), 5731-5748. doi: <https://doi.org/10.1175/JCLI-D-17-0576.1>
- Chen, S. S., & Curcic, M. (2016). Ocean surface waves in Hurricane Ike (2008) and Superstorm Sandy (2012): Coupled model predictions and observations. *Ocean Modelling*, 103, 161-176. doi: <https://doi.org/10.1016/j.ocemod.2015.08.005>
- Chen, S. S., & Houze Jr, R. A. (1997). Diurnal variation and life-cycle of deep convective systems over the tropical pacific warm pool. *Quarterly Journal of the Royal Meteorological Society*, 123(538), 357-388. doi: <https://doi.org/10.1002/qj.49712353806>
- Chen, S. S., Kerns, B. W., Guy, N., Jorgensen, D. P., Delanoë, J., Viltard, N., ... Savarin, A. (2016). Aircraft observations of dry air, the ITCZ, convective cloud systems, and cold pools in MJO during DYNAMO. *Bulletin of the American Meteorological Society*, 97(3), 405 - 423. doi: <https://doi.org/10.1175/BAMS-D-13-00196.1>
- Chen, S. S., Zhao, W., Donelan, M. A., & Tolman, H. L. (2013). Directional wind-wave coupling in fully coupled atmosphere-wave-ocean models: Results from CBLAST-Hurricane. *Journal of the Atmospheric Sciences*, 70(10), 3198 - 3215. doi: <https://doi.org/10.1175/JAS-D-12-0157.1>
- Cummings, J. A. (2005). Operational multivariate ocean data assimilation. *Quarterly Journal of the Royal Meteorological Society*, 131, 3583-3604. doi: <https://doi.org/10.1256/qj.05.105>
- Cummings, J. A., & Smedstad, O. M. (2013). Variational data assimilation for the global ocean. In S. K. Park & L. Xu (Eds.), *Data assimilation for atmospheric, oceanic and hydrologic applications (vol ii)* (chap. 13). Springer.
- DeMott, C. A., Wolding, B. O., Maloney, E. D., & Randall, D. A. (2018). Atmospheric mechanisms for MJO decay over the Maritime Continent. *Journal of Geophysical Research: Atmospheres*, 123(10), 5188-5204. doi: <https://doi.org/10.1029/2017JD026979>
- Feng, J., Li, T., & Zhu, W. (2015). Propagating and nonpropagating MJO events over Maritime Continent. *Journal of Climate*, 28(21), 8430 - 8449. doi: <https://doi.org/10.1175/JCLI-D-15-0085.1>
- Hagos, S. M., Zhang, C., Feng, Z., Burleyson, C. D., DeMott, C., Kerns, B., ... Martini, M. N. (2016). The impact of the diurnal cycle on the propa-

- gation of Madden-Julian oscillation convection across the Maritime Continent. *Journal of Advances in Modeling Earth Systems*, 8(4), 1552-1564. doi: <https://doi.org/10.1002/2016MS000725>
- Hayden, L., & Liu, C. (2021). Differences in the diurnal variation of precipitation estimated by spaceborne radar, passive microwave radiometer, and IMERG. *Journal of Geophysical Research: Atmospheres*, 126(9). doi: <https://doi.org/10.1029/2020JD033020>
- Huffman, G. J., Bolvin, D. T., Braithwaite, D., Hsu, K., Joyce, R., Kidd, C., ... Xie, P. (2019, March). *NASA global precipitation measurement (GPM) integrated multi-satellite retrievals for GPM (IMERG)* (Tech. Rep. No. ATBD v06). Greenbelt, MD, USA: National Aeronautics and Space Administration. doi: <https://doi.org/10.5067/GPM/IMERG/3B-HH/06>
- Huffman, G. J., Stocker, E. F., Bolvin, D. T., Nelkin, E. J., & Tan, J. (2019). *GPM IMERG final precipitation l3 half hourly 0.1 degree x 0.1 degree v06* [dataset]. Goddard Earth Sciences Data and Information Services Center (GES DISC). Retrieved from <ftp://arthurhou.pps.eosdis.nasa.gov/pub/gpmdata/2017/08/20/imerg/> doi: <https://doi.org/10.5067/GPM/IMERG/3B-HH/06>
- Inness, P. M., & Slingo, J. M. (2006). The interaction of the Madden-Julian Oscillation with the Maritime Continent in a GCM. *Quarterly Journal of the Royal Meteorological Society*, 132(618), 1645-1667. doi: <https://doi.org/10.1256/qj.05.102>
- Kerns, B. W., & Chen, S. S. (2016). Large-scale precipitation tracking and the MJO over the Maritime Continent and Indo-Pacific warm pool. *Journal of Geophysical Research: Atmospheres*, 121, 8755-8776. doi: <https://doi.org/10.1002/2015JD024661>
- Kerns, B. W., & Chen, S. S. (2020). A 20-year climatology of Madden-Julian oscillation convection: Large-scale precipitation tracking from TRMM-GPM rainfall. *Journal of Geophysical Research: Atmospheres*, 124. doi: <https://doi.org/10.1029/2019JD032142>
- Kikuchi, K., & Wang, B. (2008). Diurnal precipitation regimes in the global tropics. *Journal of Climate*, 21(11), 2680-2696. doi: <https://doi.org/10.1175/2007JCLI2051.1>
- Lee, Y.-C., & Wang, Y.-C. (2021). Evaluating diurnal rainfall signal performance from CMIP5 to CMIP6. *Journal of Climate*, 34(18), 7607 - 7623. doi: <https://doi.org/10.1175/JCLI-D-20-0812.1>
- Li, Y., Jourdain, N. C., Taschetto, A. S., Gupta, A. S., Argüeso, D., Masson, S., & Cai, W. (2017). Resolution dependence of the simulated precipitation and diurnal cycle over the Maritime Continent. *Climate Dynamics*, 48, 4009-4028. doi: <https://doi.org/10.1007/s00382-016-3317-y>
- Ling, J., Zhang, C., Joyce, R., Xie, P.-P., & Chen, G. (2019). Possible role of the diurnal cycle in land convection in the barrier effect on the MJO by the Maritime Continent. *Geophysical Research Letters*, 46(5), 3001-3011. doi: <https://doi.org/10.1029/2019GL081962>
- Ling, J., Zhao, Y., & Chen, G. (2019). Barrier effect on MJO propagation by the Maritime Continent in the MJO Task Force/GEWEX atmospheric system study models. *Journal of Climate*, 32(17), 5529 - 5547. doi: <https://doi.org/10.1175/JCLI-D-18-0870.1>
- Love, B. S., Matthews, A. J., & Lister, G. M. S. (2011). The diurnal cycle of precipitation over the Maritime Continent in a high-resolution atmospheric model. *Quarterly Journal of the Royal Meteorological Society*, 137(657), 934-947. doi: <https://doi.org/10.1002/qj.809>
- Lu, J., Li, T., & Wang, L. (2019). Precipitation diurnal cycle over the Maritime Continent modulated by the MJO. *Climate Dynamics*, 53.
- Madden, R. A., & Julian, P. R. (1971). Detection of a 40-50 day oscillation in the zonal wind in the tropical Pacific. *Journal of Atmospheric Sciences*, 28(5),

- 702 - 708. doi: [https://doi.org/10.1175/1520-0469\(1971\)028<0702:DOADOI>2.0.CO;2](https://doi.org/10.1175/1520-0469(1971)028<0702:DOADOI>2.0.CO;2)
- Madden, R. A., & Julian, P. R. (1972). Description of global-scale circulation cells in the tropics with a 40–50 day period. *Journal of Atmospheric Sciences*, 29(6), 1109 - 1123. doi: [https://doi.org/10.1175/1520-0469\(1972\)029<1109:DOGSCC>2.0.CO;2](https://doi.org/10.1175/1520-0469(1972)029<1109:DOGSCC>2.0.CO;2)
- Mazza, E., & Chen, S. S. (2022). Tropical cyclone rainfall climatology, extremes and flooding potential over the continental US. *Submitted to the Journal of Hydrometeorology*.
- Mechem, D. B., Houze Jr, R. A., & Chen, S. S. (2002). Layer inflow into precipitating convection over the western tropical pacific. *Quarterly Journal of the Royal Meteorological Society*, 128(584), 1997-2030. doi: <https://doi.org/10.1256/003590002320603502>
- Metzger, E. J., Smedstad, O. M., Thoppil, P. G., Hurlburt, H. E., Cummings, J. A., Wallcraft, A. J., ... DeHaan, C. J. (2014, September). US navy operational global ocean and arctic ice prediction systems. *Oceanography*, 27(3), 32-43. doi: <https://doi.org/10.5670/oceanog.2014.66>
- Miller, S. T. K., Keim, B. D., Talbot, R. W., & Mao, H. (2003). Sea breeze: Structure, forecasting, and impacts. *Reviews of Geophysics*, 41(3). doi: <https://doi.org/10.1029/2003RG000124>
- Moron, V., Robertson, A. W., Qian, J.-H., & Ghil, M. (2015). Weather types across the Maritime Continent: from the diurnal cycle to interannual variations. *Frontiers in Environmental Science*, 2. doi: <https://doi.org/10.3389/fenvs.2014.00065>
- Neale, R., & Slingo, J. (2003). The Maritime Continent and its role in global climate: A GCM study. *Journal of Climate*, 16(5), 834-848. doi: [https://doi.org/10.1175/1520-0442\(2003\)016<0834:TMCAIR>2.0.CO;2](https://doi.org/10.1175/1520-0442(2003)016<0834:TMCAIR>2.0.CO;2)
- Nesbitt, S. W., & Zipser, E. J. (2003). The diurnal cycle of rainfall and convective intensity according to three years of TRMM measurements. *Journal of Climate*, 16(10), 1456 - 1475. doi: [https://doi.org/10.1175/1520-0442\(2003\)016<1456:TDCORA>2.0.CO;2](https://doi.org/10.1175/1520-0442(2003)016<1456:TDCORA>2.0.CO;2)
- NOAA National Geophysical Data Center. (2009). *ETOPO1 1 arc-minute global relief model* [dataset]. NOAA National Centers for Environmental Information. Retrieved from <https://www.ngdc.noaa.gov/mgg/global/> doi: <https://doi.org/10.7289/V5C8276M>
- Oh, J.-H., Kim, B.-M., Kim, K.-Y., Song, H.-J., & Lim, G.-H. (2013). The impact of the diurnal cycle on the MJO over the Maritime Continent: a modeling study assimilating TRMM rain rate into global analysis. *Climate Dynamics*, 40(3), 893-911. doi: <https://doi.org/10.1007/s00382-012-1419-8>
- Oh, J.-H., Kim, K.-Y., & Lim, G.-H. (2012). Impact of MJO on the diurnal cycle of rainfall over the western Maritime Continent in the austral summer. *Climate Dynamics*, 38(5), 1167-1180. doi: <https://doi.org/10.1007/s00382-011-1237-4>
- Peatman, S. C., Matthews, A. J., & Stevens, D. P. (2014). Propagation of the Madden-Julian Oscillation through the Maritime Continent and scale interaction with the diurnal cycle of precipitation. *Quarterly Journal of the Royal Meteorological Society*, 140(680), 814-825. doi: <https://doi.org/10.1002/qj.2161>
- Ramage, C. S. (1968). Role of a tropical "Maritime Continent" in the atmospheric circulation. *Monthly Weather Review*, 96(6), 365-370.
- Rauniyar, S. P., & Walsh, K. J. E. (2011). Scale interaction of the diurnal cycle of rainfall over the Maritime Continent and Australia: Influence of the MJO. *Journal of Climate*, 24(2), 325 - 348. doi: <https://doi.org/10.1175/2010JCLI3673.1>
- Sakaeda, N., Kiladis, G., & Dias, J. (2017). The diurnal cycle of tropical cloudiness and rainfall associated with the Madden-Julian Oscillation. *Journal of Climate*.

- 773 Savarin, A., & Chen, S. S. (2022a). Pathways to better prediction of the MJO. 1.  
774 Effects of model resolution and moist physics on atmospheric boundary layer  
775 and precipitation. *Journal of Advances in Modeling Earth Systems*. doi:  
776 <https://doi.org/10.1029/2021MS002929>
- 777 Savarin, A., & Chen, S. S. (2022b). Pathways to better prediction of the  
778 MJO. 2. Impacts of atmosphere-ocean coupling on the upper ocean and  
779 MJO propagation. *Journal of Advances in Modeling Earth Systems*. doi:  
780 <https://doi.org/10.1029/2021MS002928>
- 781 Schiemann, R., Demory, M.-E., Mizieliński, M. S., Roberts, J. M., Shaffrey, L. C.,  
782 Strachan, J., & Vidale, P. L. (2014). The sensitivity of the tropical circulation  
783 and Maritime Continent precipitation to climate model resolution. *Climate*  
784 *Dynamics*, 42, 2455-2468. doi: <https://doi.org/10.1007/s00382-013-1997-0>
- 785 Skamarock, W. C., Klemp, J. B., Dudhia, J., Gill, D. O., Barker, D. M., Duda, M.,  
786 ... Powers, J. G. (2008). *A description of the advanced research WRF ver-*  
787 *sion 3* (Tech. Rep. Nos. NCAR/TN-475+STR). University Corporation for  
788 Atmospheric Research. doi: <https://doi.org/10.5065/D68S4MVH>
- 789 Sobel, A. H., Maloney, E. D., Bellon, G., & Frierson, D. M. (2010). Surface fluxes  
790 and tropical intraseasonal variability: a reassessment. *Journal of Advances in*  
791 *Modeling Earth Systems*, 2(1). doi: <https://doi.org/10.3894/JAMES.2010.2.2>
- 792 Tan, H., Ray, P., Barrett, B., Dudhia, J., Moncrieff, M., Zhang, L., & Zermeno-Diaz,  
793 D. (2022). Understanding the role of topography on the diurnal cycle of  
794 precipitation in the Maritime Continent during MJO propagation. *Climate Dy-*  
795 *namics*, 58(11), 3003-3019. doi: <https://doi.org/10.1007/s00382-021-06085-0>
- 796 Tan, J., Huffman, G. J., Bolvin, D. T., & Nelkin, E. J. (2019). Diurnal cycle of  
797 IMERG V06 precipitation. *Geophysical Research Letters*, 46(22), 13584-13592.  
798 doi: <https://doi.org/10.1029/2019GL085395>
- 799 Tian, B., Waliser, D. E., & Fetzner, E. J. (2006). Modulation of the diurnal cycle  
800 of tropical deep convective clouds by the MJO. *Geophysical Research Letters*,  
801 33(20). doi: <https://doi.org/10.1029/2006GL027752>
- 802 Tian, F., Hou, S., Yang, L., Hu, H., & Hou, A. (2018). How does the evalua-  
803 tion of the GPM IMERG rainfall product depend on gauge density and  
804 rainfall intensity? *Journal of Hydrometeorology*, 19(2), 339 - 349. doi:  
805 <https://doi.org/10.1175/JHM-D-17-0161.1>
- 806 Wang, S., Sobel, A. H., Lee, C.-Y., Ma, D., Chen, S. S., Curcic, M., & Pullen, J.  
807 (2021). Propagating mechanisms of the 2016 summer BSISO event: Air-sea  
808 coupling, vorticity, and moisture. *Journal of Geophysical Research: Atmo-*  
809 *spheres*, 126(2), e2020JD033284. doi: <https://doi.org/10.1029/2020JD033284>
- 810 Watters, D., Battaglia, A., & Allan, R. P. (2021). The diurnal cycle of precipitation  
811 according to multiple decades of global satellite observations, three CMIP6  
812 models, and the ECMWF reanalysis. *Journal of Climate*, 34(12), 5063 - 5080.  
813 doi: <https://doi.org/10.1175/JCLI-D-20-0966.1>
- 814 Wei, Y., Pu, Z., & Zhang, C. (2020). Diurnal cycle of precipitation over the Mar-  
815 itime Continent under modulation of MJO: Perspectives from cloud-permitting  
816 scale simulations. *Journal of Geophysical Research: Atmospheres*, 125(13). doi:  
817 <https://doi.org/10.1029/2020JD032529>
- 818 Wentz, F. J., Scott, J., Hoffman, R., Leidner, M., Atlas, R., & Artizzone, J. (2015).  
819 *Remote sensing systems cross-calibrated multi-platform (CCMP) 6-hourly*  
820 *ocean vector wind analysis product on 0.25 deg grid, version 2.0* [dataset]. Re-  
821 mote Sensing Systems. Retrieved from [www.remss.com/measurements/ccmp](http://www.remss.com/measurements/ccmp)  
822 doi: <https://doi.org/10.7289/V5C8276M>
- 823 Wheeler, M. C., & Hendon, H. H. (2004). An all-season real-time multivariate  
824 MJO index: Development of an index for monitoring and prediction. *Monthly*  
825 *Weather Review*, 132(8), 1917 - 1932. doi: 10.1175/1520-0493(2004)132<1917:  
826 AARMMI>2.0.CO;2
- 827 Wu, C.-H., & Hsu, H.-H. (2009). Topographic influence on the MJO in the Mar-

- itime Continent. *Journal of Climate*, 22(20), 5433-5448. doi: <https://doi.org/10.1175/2009JCLI2825.1>
- Zhang, C., & Ling, J. (2017). Barrier effect of the Indo-Pacific Maritime Continent on the MJO: Perspectives from tracking MJO precipitation. *Journal of Climate*, 30(9), 3439 - 3459. doi: <https://doi.org/10.1175/JCLI-D-16-0614.1>
- Zhang, C., Wang, Y., & Hamilton, K. (2011). Improved representation of boundary layer clouds over the southeast pacific in ARW-WRF using a modified Tiedtke cumulus parameterization scheme. *Monthly Weather Review*, 139(11), 3489 - 3513. doi: <https://doi.org/10.1175/MWR-D-10-05091.1>
- Zhang, L., & Han, W. (2020). Barrier for the eastward propagation of Madden-Julian oscillation over the Maritime Continent: A possible new mechanism. *Geophysical Research Letters*, 47(21). doi: <https://doi.org/10.1029/2020GL090211>
- Zhou, Y., Fang, J., & Wang, S. (2021). Impact of islands on the MJO propagation across the Maritime Continent: a numerical modeling study of an MJO event. *Climate Dynamics*, 57(9). doi: 10.1007/s00382-021-05849-y